

# Hindrance of $^{16}\text{O}+^{208}\text{Pb}$ fusion at extreme sub-barrier energies

Henning Esbensen

*Physics Division, Argonne National Laboratory, Argonne, Illinois 60439*

Șerban Mișicu

*National Institute for Nuclear Physics,*

*Bucharest, P. O. Box MG6, Romania*

(Dated: February 2, 2008)

## Abstract

We analyze the fusion data for  $^{16}\text{O}+^{208}\text{Pb}$  using coupled-channels calculations. We include couplings to the low-lying surface excitations of the projectile and target and study the effect of the ( $^{16}\text{O},^{17}\text{O}$ ) one-neutron pickup. The hindrance of the fusion data that is observed at energies far below the Coulomb barrier cannot be explained by a conventional ion-ion potential and defining the fusion in terms of ingoing-wave boundary conditions (IWBC). We show that the hindrance can be explained fairly well by applying the M3Y double-folding potential which has been corrected with a calibrated, repulsive term that simulates the effect of nuclear incompressibility.

We show that the coupling to one-neutron transfer channels plays a crucial role in improving the fit to the data. The best fit is achieved by increasing the transfer strength by 25% relative to the strength that is required to reproduce the one-neutron transfer data. The larger strength is not unrealistic because the calculated inelastic plus transfer cross section is in good agreement with the measured quasielastic cross section. We finally discuss the problem of reproducing the fusion data at energies far above the Coulomb barrier. Here we do not account for the data when we apply the IWBC but the discrepancy is essentially eliminated by applying the M3Y+repulsion potential and a weak, short-ranged imaginary potential.

PACS numbers: 24.10.Eq, 25.60.Pj, 25.70.-z

## I. INTRODUCTION

It would be desirable to be able to make a consistent coupled-channels calculation of the most important reaction channels in  $^{16}\text{O}$  on  $^{208}\text{Pb}$  collisions at energies near and below the Coulomb barrier. This has been attempted several times in the past [1, 2, 3] but the analyses were never completely satisfactory. For example, it was difficult to reproduce the energy dependence of the measured fusion cross section [4, 5]. In order to improve the fit to the data it was necessary either to use a very small diffuseness of the ion-ion potential [1] or to use a complex ion-ion potential in the calculations [2, 3]. Both modifications indicate that the calculations were either incomplete in terms of the reaction channels that were considered or that other features of the calculations were unrealistic.

The old  $^{16}\text{O}+^{208}\text{Pb}$  fusion data [4, 5] turned out to contain some uncertainties, in particular with respect to the evaporation residue component (see Ref. [6]). The most accurate data that are now available can be found in Ref. [7]. The analysis of the revised data showed that there are still some inconsistencies with coupled-channels calculations. Thus it was necessary to use a large diffuseness of the ion-ion potential in order to reproduce the fusion data at energies above the Coulomb barrier, whereas the fusion barrier distribution extracted from the data required a very small diffuseness.

We have recently pointed out [8] that many of the ion-ion potentials, which have been used in the past, are unrealistic at small distances between the reacting nuclei. While the ion-ion potential apart for minor adjustments is quite accurately given by the M3Y double-folding potential at larger distances (say, outside the Coulomb barrier), this potential is unrealistic at smaller distances, where it produces a pocket in the entrance channel potential that is far too deep, sometimes even deeper than the ground state energy of the compound nucleus. By considering the effect of nuclear incompressibility we obtained what we think is a more realistic interaction, which we call the M3Y+repulsion potential. It produces a rather shallow pocket in the entrance channel potential [8]. Such a shallow pocket makes it possible to accurately reproduce the measured fusion cross sections for  $^{64}\text{Ni}+^{64}\text{Ni}$  [9], in particular at the lowest energies, where the data fall off steeply with decreasing energy. The steep falloff is referred to as the fusion hindrance; see Ref. [10] for a recent discussion of this phenomenon.

The measurements of the fusion of  $^{16}\text{O}+^{208}\text{Pb}$  [7] were recently extended to very small

cross sections [11]. The new data exhibit a fusion hindrance at low energies which is similar to what has been observed for many other heavy-ion systems [10]. It is therefore of interest to see whether the M3Y potential, corrected for nuclear incompressibility as discussed above, can account for the new data when applied in coupled-channels calculations. It is also of interest to investigate whether the M3Y+repulsion potential can explain the suppression of the high-energy fusion data which was discussed in Ref. [12].

The coupled-channels calculations that have been performed previously [1, 2, 3, 7] included couplings to the  $2^+$ ,  $3^-$ , and  $5^-$  low-lying states in  $^{208}\text{Pb}$ , the lowest  $3^-$  state in  $^{16}\text{O}$ , and to transfer channels [ $(^{16}\text{O}, ^{17}\text{O})$  neutron pickup and  $(^{16}\text{O}, ^{15}\text{N})$  proton stripping]. The reaction data [4] had a significant yield of C isotopes, which were simulated by simplified couplings in some of the the calculations [1, 3]. The calculations showed that the couplings to the transfer channels have a significant effect on the calculated fusion cross sections and improve the fit to the data.

We include in our analysis of the  $^{16}\text{O}+^{208}\text{Pb}$  fusion data [7, 11] some of the most important surface excitation modes and study the effect of the  $(^{16}\text{O}, ^{17}\text{O})$  neutron pickup reaction, which is one of the most dominant reaction channels besides fusion [4, 13]. We also study how well we can account for the total reaction cross section and the elastic scattering data [4].

## II. DESCRIPTION OF THE CALCULATIONS

The coupled-channels calculations we perform are similar to those discussed in Refs. [14, 15]. Here we summarize the approximations we make and describe the input to the calculations. The basic assumption is the rotating frame approximation, which implies that one has to include only one channel for each state of spin  $I$ , and not the  $I+1$  (or even  $2I+1$ ) channels that are required in general. This approximation is commonly used in calculations of heavy-ion fusion cross sections because it makes it possible to include the effect of many reaction channels. It is a reliable approximation for calculating fusion and elastic scattering but the angular distributions for inelastic scattering and transfer reactions can be poor, in particular at forward angles (see, for example, Ref. [14]).

### A. Ion-ion potentials

The ion-ion potentials we use are the same as those we applied in Ref. [16], namely, the Aküyz-Winther (AW) and the M3Y+repulsion double-folding potential. The AW potential is defined by Eqs. (40,41,44,45) in Sect. III.1 of Ref. [17] but we have modified Eq. (40) by introducing an adjustable radius parameter  $\Delta R$ ,

$$U_{12}^N(r) = \frac{-16\pi\gamma R_{12}a}{1 + \exp((r - R_1 - R_2 - \Delta R)/a)}. \quad (1)$$

Here  $\gamma = 0.95 \text{ MeV/fm}^2$  is the nuclear surface tension,  $a$  is the surface diffuseness defined in Eq. (44), Sect. III.1 of Ref. [17],  $R_i = 1.2A_i^{1/3} - 0.09 \text{ fm}$ , and  $R_{12} = R_1 R_2 / (R_1 + R_2)$ . The parameter  $\Delta R$  is adjusted so that the two potentials, namely, the AW and the M3Y+repulsion potentials, produce the same Coulomb barrier height. In the case discussed below this requires the value  $\Delta R = 0.13 \text{ fm}$ .

The M3Y double-folding potential is calculated numerically in the Fourier representation,

$$U(r) = \frac{1}{2\pi^2} \int q^2 dq \rho_1(q) \rho_2(q) v(q) j_0(qr). \quad (2)$$

Here  $v(q)$  represents the M3Y effective nucleon-nucleon interaction,  $j_0(x)$  is the spherical Bessel function, and  $\rho_i(q)$  is the Fourier transform of the density of nucleus  $i$ . The Yukawa and contact type interactions that we use [16] to define the direct and exchange part of the M3Y interaction have simple analytic Fourier transforms.

The densities are parametrized in terms of a Fermi function. We use the proton and neutron density parameters:  $R_p = 2.53$ ,  $R_n = 2.57$ ,  $a=0.513 \text{ fm}$  for  $^{16}\text{O}$ , and  $R_p = 6.60$ ,  $R_n = 6.75$ ,  $a=0.546 \text{ fm}$  for  $^{206}\text{Pb}$ . The proton densities are consistent with the measured charge densities [18] while the radii for the neutron densities are slightly larger. The Fermi function does not have a simple analytic Fourier transform so we use instead an accurate analytic approximation, which has an exact analytic Fourier transform. This approximation is described in the appendix.

The repulsive interaction, which simulates the effect of the nuclear incompressibility (see Ref. [16] for details) is calculated from the same integral, Eq. (2). In this case the  $v(q)$  represents the (constant) Fourier transform of a contact interaction with the strength  $V_{rep}$ . The densities we use in the integral have the same radii as those used in the calculation of the M3Y double-folding potential but the diffuseness  $a_{rep}$  is chosen differently. We have chosen

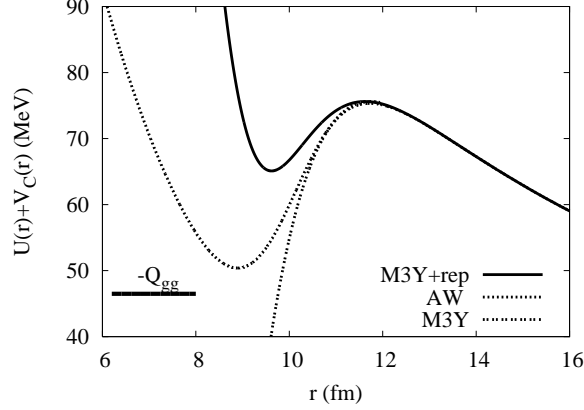


FIG. 1: The M3Y and M3Y+repulsion potentials are compared to the AW potential. The height of the Coulomb barrier is 75.6 MeV in all three cases.

the parameters  $V_{rep} = 570 \text{ MeV fm}^3$  and  $a_{rep} = 0.35 \text{ fm}$  and obtain a nuclear incompressibility of 245 MeV. The total potential (M3Y+repulsion plus Coulomb interaction) is illustrated by the solid curve in Fig. 1. It has a Coulomb barrier of 75.6 MeV and the minimum energy of the pocket is 65.1 MeV. The latter pocket energy was chosen because it is required by the fusion data as we shall see later on, and this was achieved by adjusting  $a_{rep}$ .

The AW potential, Eq. (1), with  $\Delta R = 0.13 \text{ fm}$  adjusted to produce the same Coulomb barrier height as the M3Y+repulsion potential, is also shown in Fig. 1. It has a pocket energy at 50.5 MeV. The total potential which is based on the pure (direct+exchange) M3Y potential has a much deeper pocket. It is unrealistic because the minimum is lower than the ground state energy of the compound nucleus  $^{224}\text{Th}$ , which is indicated in the figure by the thick solid, horizontal line at  $-Q_{gg} = 46.5 \text{ MeV}$ .

## B. Surface excitations

The structure input that will be used to describe the excitation of the low-lying states in  $^{16}\text{O}$  and  $^{208}\text{Pb}$  is given in Table I. For the lead states it is assumed that the Coulomb and nuclear  $\beta$ -values are identical. For the oxygen states we use the parameters that were determined in Ref. [19]. The coupling strengths to the oxygen states are rather strong, in particular for the octupole state, but the strengths for Coulomb excitation are consistent with the adopted values [20]. In addition to the states shown in Table I we also include all mutual excitations of these states up to an excitation energy cutoff of 7.7 MeV. That gives

TABLE I: Structure input for  $^{16}\text{O}$  [19, 20] and  $^{208}\text{Pb}$  [20] The quadrupole moments of the  $2^+$  and  $3^-$  states in  $^{208}\text{Pb}$ ,  $Q = -0.7(3)$  and  $-0.34(15)$  b [21], respectively, have been converted into an effective quadrupole deformation  $\beta(Q)$ .

Nucleus	$\lambda^\pi$	$E_x$ (MeV)	$B(E\lambda)$ (W.u.)	$\beta_\lambda^C$	$\beta_\lambda^N$	$\beta(Q)$
$^{16}\text{O}$	$2^+$	6.92	3.1(1)	0.352	0.324	-
	$3^-$	6.13	13.5(7)	0.713	0.481	-
$^{208}\text{Pb}$	$3^-$	2.615	33.9(5)	0.111	0.111	0.038
	$5^-$	3.198	11.0(7)	0.059	0.059	-
	$2^+$	4.085	8.7(5)	0.057	0.057	0.078
	$4^+$	4.323	18.0(13)	0.079	0.079	-

a total of 12 channels.

As in our previous work [16] we include all couplings up to second order in the nuclear deformation parameters, whereas Coulomb excitation is described by linear couplings. The form factors for the linear and quadratic nuclear couplings are assumed to be the first and second radial derivatives of the ion-ion potential, respectively.

### C. Neutron transfer

We will also study the effect of transfer and consider explicitly the one-neutron transfer to the  $5/2^+$  ground state of  $^{17}\text{O}$  leaving the  $^{207}\text{Pb}$  nucleus in the  $1/2^-$  ground state, and in the  $5/2^-$  and  $3/2^-$  excited states at 0.57 and 0.88 MeV, respectively. The Q-values for these transfers are -3.22 MeV, -3.79, and -4.10 MeV. These transfer channels dominate the measured ( $^{16}\text{O}, ^{17}\text{O}$ ) cross section at 104 MeV lab energy [13], and the spectroscopic factors that were extracted are close to one. The three transfer channels are lumped together into one effective transfer channel, the same way it was done in Ref. [14]. The effective Q-value for the transfer is set to  $Q_{eff} = -3.2$  MeV. This represents a weighted average of the actual Q-values corrected as suggested in Ref. [22] for the lower Coulomb barrier ( $\Delta V_{CB} = 0.46$  MeV) in the transfer channel, i. e.,

$$Q_{eff} = \frac{\sum Q_n \sigma_n}{\sum \sigma_n} + \Delta V_{CB}. \quad (3)$$

Here the sums over  $N$  are over the three final states mentioned above.

The transfer form factors we use are taken from Ref. [23] and they are calculated for full spectroscopic strength. The overall strength of the effective form factor will be scaled by the factor  $F_{1n}$ , in order to be able to reproduce the measured transfer data [13] at 104 MeV in the laboratory frame. We shall see later on (Fig. 3B) that this requires the strength  $F_{1n} = 0.95$ , whereas boosting the strength to  $F_{1n} \approx 1.2$  makes it possible to simulate the total reaction cross section.

### III. RESULTS OF THE CALCULATIONS

The coupled-channels equations are solved with the usual scattering conditions at large distances and ingoing-wave boundary conditions (IWBC) that are imposed at the location  $R_{\text{pocket}}$  of minimum of the potential pocket in the entrance channel. We found in Ref. [16] that the fusion hindrance observed at extreme subbarrier energies could only be explained by defining the fusion in terms of IWBC. However, in order to be able to simulate the fusion and the total reaction cross section at energies far above the Coulomb barrier we will also consider the possibility of supplementing the IWBC with an imaginary potential.

#### A. Fusion

The measured fusion cross sections [7, 11] are compared in Figs. 2A and 2B to the results of coupled-channels calculations that are based on the AW and M3Y+repulsion potentials, respectively. In each case we show in increasing order the fusion cross sections we obtain in the no-coupling limit, by including couplings to the one-neutron transfer (ntr), and to excitations of the surface modes (exc). The solid curves show the combined effect of surface excitations and one-neutron transfer. It is seen that the full calculation (solid curve) in Fig. 2B, which is based on the M3Y+repulsion potential, provides the best fit to the data, in particular at the lowest energies where the 7 new data points [11] are shown by solid points.

The best  $\chi^2$  per point we obtain by shifting the calculation by an energy  $\Delta E$  is shown in Table II as a function of the transfer strength  $F_{1n}$ . It is seen that the quality of the fit to the data is insensitive to the transfer strength when the calculations are based on the AW potential, whereas the fit improves considerably with increasing transfer strength when the M3Y+repulsion potential is used. The best fit is achieved for  $F_{1n} \approx 1.2$ .

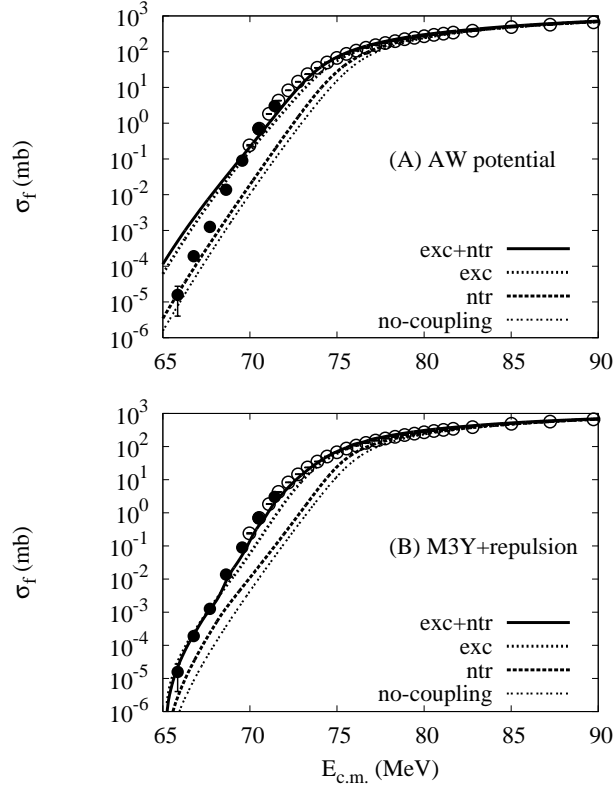


FIG. 2: Calculated fusion cross sections, obtained with the AW potential (A) and the M3Y+repulsion potential (B), are compared with the data of Ref. [7] (open circles) and Ref. [11] (solid points). The curves show in increasing order the no-coupling limit, the coupled-channels results for neutron transfer only (ntr) using  $F_{1n} = 0.95$ , for surface excitations only (exc), and the combined effect of surface excitations and transfer (exc+ntr, solid curve).

It is also seen in Table II that the fit to all of the data points is very poor when the AW potential is used, whereas the  $\chi^2/N$  is much smaller when the calculations are based on the M3Y+repulsion potential. We assumed in our analysis a 5% systematic error in addition to the statistical uncertainty. However, it is not clear whether this assumption is realistic. Another way of expressing the quality of the best fit is to say that it requires a 12% uncertainty, in addition to the statistical error, in order to produce a  $\chi^2/N \approx 1$ .

## B. Reaction cross sections

In this subsection we take a look at the measured reaction and transfer cross sections [4, 13] in order to determine a realistic value of the transfer coupling strength  $F_{1n}$ . The



TABLE II: Analysis of  $^{16}\text{O}+^{208}\text{Pb}$  fusion data. The best  $\chi^2/N$ , and the energy shift  $\Delta E$  of the calculations that is required to minimized the  $\chi^2$ , are shown for two data sets. The analysis included statistical errors and an assumed systematic error of 5%. The calculations were based on the AW potential and the M3Y+repulsion potentials, respectively, and included couplings to surface modes and one-neutron transfer using different values of the transfer coupling strength  $F_{1n}$ .

Potential	$F_{1n}$	Old data [7]		All data [7, 11]	
		$\Delta E$ MeV	$\chi^2/N$	$\Delta E$ MeV	$\chi^2/N$
AW	0	-0.41	9.9	0.50	72
	0.95	-0.24	9.2	0.70	73
	1.2	-0.06	9.2	0.82	72
M3Y + repulsion	0	-0.61	14.2	-0.45	25.6
	0.95	-0.20	7.2	-0.20	7.1
	1.10	-0.08	5.7	-0.10	5.6
	1.20	0.0	5.2	0.015	5.2
	1.30	0.1	5.8	0.10	5.4

reaction data are compared in Fig. 3 to calculations that are based on the M3Y+repulsion potential and include couplings to surface excitations and one-neutron transfer with the coupling strength  $F_{1n} = 0.95$ . The results shown in Fig. 3A were obtained without using any imaginary potential, i. e., the only absorption in this case is the fusion which is determined by the IWBC. The top solid curve is the total reaction cross section which falls below the data [4] (top solid points) so there is obviously room for more reaction channels.

The next set of data points in Fig. 3A are the fusion cross sections (open circles) which are reproduced fairly well by the calculation (upper dashed curve). The diamonds show the difference between the measured total reaction and the quasielastic cross sections. They agree very well with the measured fusion cross cross sections, so the total reaction cross section is essentially comprised of fusion and quasielastic scattering.

The triangles in Fig. 3A are the measured cross sections for oxygen like fragments, i. e., the sum of the inelastic and neutron transfer cross sections. These data points are slightly below the calculated values (lower dashed curve). The lowest star-like point at 96.6 MeV is the one-neutron cross section obtained in Ref. [13] and it is also slightly below the calculated

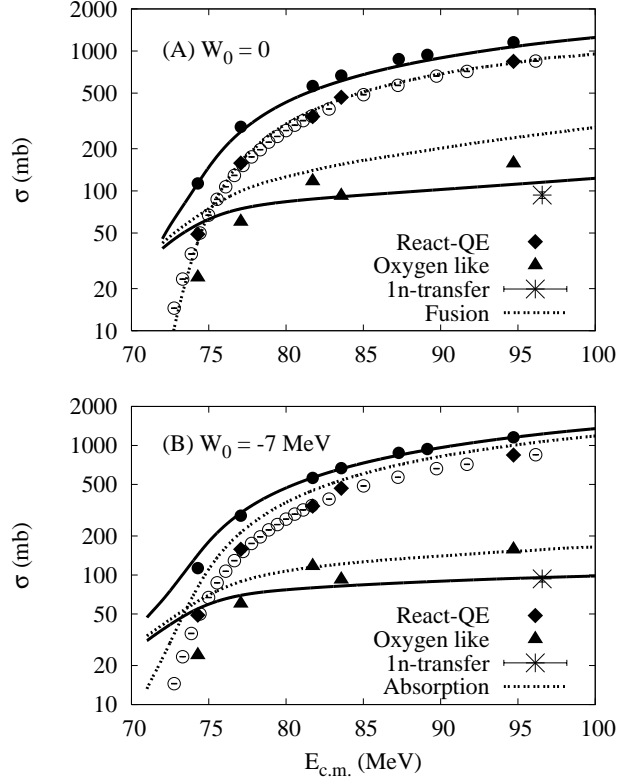


FIG. 3: Calculated reaction cross sections (top solid curves) are compared to data (solid points) [4]. The calculations are based on the M3Y+repulsion potential and include couplings to surface excitations and neutron transfer with  $F_{1n} = 0.95$ . The calculations in (A) use IWBC, whereas (B) employs an imaginary potential. In decreasing order we also show the cross sections for fusion (open circles), oxygen like fragments (triangles), and one-neutron transfer (star). The diamonds are the difference between the measured reaction and quasielastic cross sections.

cross section (the lower solid curve).

A simple way to simulate the reaction data in Fig. 3 is to increase the transfer coupling strength  $F_{1n}$ . Thus we find that we need a value in the range of  $F_{1n} \approx 1.2 - 1.3$  in order to reproduce the total reaction cross section at the higher energies. It is interesting that this coupling strength is roughly what produces the best fit to the fusion data according to Table II. This implies that the calculated surface excitation plus one-neutron transfer cross section accounts in this case for the experimental quasielastic cross section.

Another way to account for the total reaction cross section is to employ a complex ion-ion potential. We find that the total reaction cross section can be simulated quite well by including in the calculations an imaginary potential of the Woods-Saxon type with the

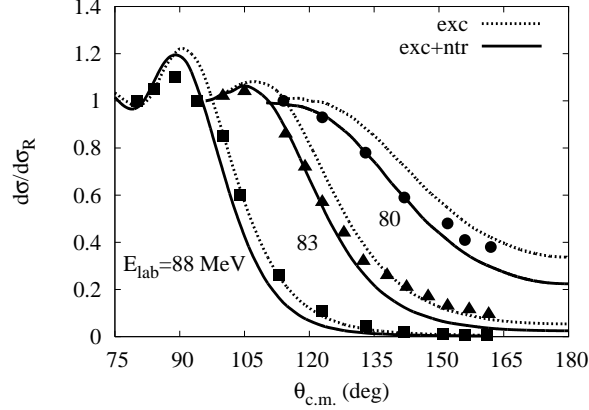


FIG. 4: Elastic scattering data at  $E_{lab} = 80, 83,$  and  $88$  MeV [4] are compared with calculations that are based on the M3Y+repulsion and the imaginary potential discussed in the text. The dashed curves (exc) include the effect of surface excitations. The solid curves (exc+ntr) include in addition the effect of neutron transfer using the strength  $F_{1n} = 0.95$ .

parameters:  $W_0 = -7$  MeV,  $R_w = 11$  fm, and  $a_w = 0.45$  fm. The results are shown in Fig. 3B. The absorption cross section (upper dashed curve) exceeds the measured fusion cross section because it must now simulate the sum of fusion and charged-particle transfer. The calculated cross section for oxygen-like fragments (lower dashed curve) is in good agreement with the data (triangles). The measured one-neutron transfer cross section at  $96.6$  MeV [13] (the star-like symbol) is also reproduced by the calculation (the lower solid curve). This was achieved as mentioned earlier by adjusting the coupling strength to  $F_{1n} = 0.95$ .

### C. Elastic scattering

The elastic scattering cross sections we obtain are compared with data [4] in Fig. 4. The calculations include the diagonal imaginary potential ( $W_0 = -7$  MeV,  $a_w = 0.45$  fm,  $R_w = 11$  fm) which was calibrated in the previous subsection so that the total reaction cross section was reproduced. The dashed curves are based on couplings to surface excitations (exc). The solid curves include in addition the effect of transfer (exc+ntr) and they are seen to reproduce the data at the lowest energies. Some discrepancies develop at the highest energy where the calculated rainbow peak is too high and the large angle scattering cross section is too low. This is somewhat disappointing because the imaginary potential and the transfer strength  $F_{1n}$  were adjusted in the previous subsection to account for the measured cross

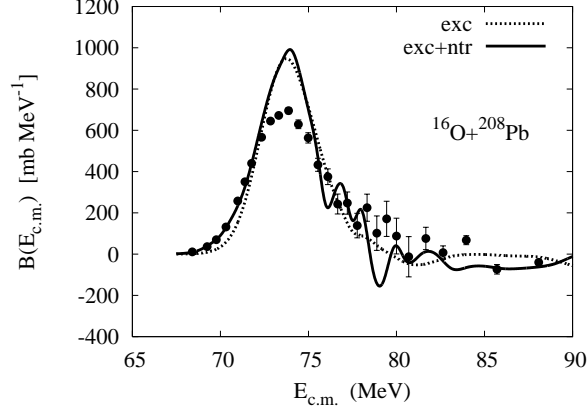


FIG. 5: Barrier distributions extracted from the data and from calculations that are based on the M3Y+repulsion potential. Both calculations include couplings to surface excitations (exc). The solid curve (exc+ntr) includes in addition the coupling to neutron transfer with the coupling strength  $F_{1n}=1.2$ .

sections, c. f. Fig. 3B.

#### D. Barrier distribution and $S$ factor

A good way to focus on the energy dependence of the fusion cross section at energies close to the Coulomb barrier is to plot the so-called barrier distribution, which is defined as the second derivative of the energy weighted fusion cross section [24]

$$B(E_{c.m.}) = \frac{d^2(E_{c.m.}\sigma_f(E_{c.m.}))}{dE_{c.m.}^2}. \quad (4)$$

The results we obtain, with and without the effect of transfer, are compared in Fig. 5 to the barrier distribution we have extracted from the data. The most obvious discrepancy with the data is the much higher peak of the calculated distributions. The same problem was recognized in the coupled-channels calculations presented in Ref. [7]. There the discrepancy was removed by applying a very small diffuseness ( $a \approx 0.4$  fm) of the ion-ion potential but that would be inconsistent with the high-energy behavior of the fusion cross section which required a large diffuseness ( $a \approx 1$  fm) [7]. It is unfortunate that using the shallow entrance channel potential we obtain with the M3Y+repulsion double-folding potential does not resolve the discrepancy with the peak height of the experimental barrier distribution.

A significant difference between the two calculations shown in Fig. 5 is the behavior at

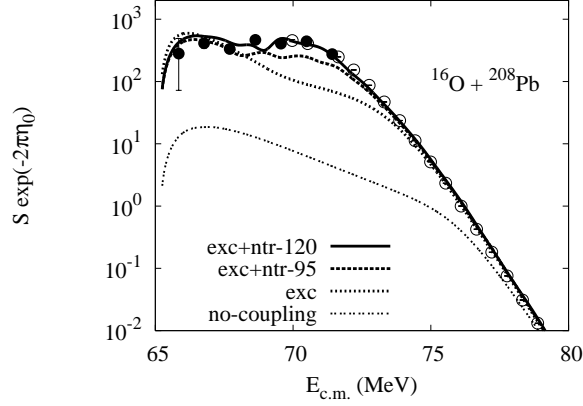


FIG. 6: Calculated  $S$  factors for fusion (scaled by the factor  $\exp(-2\pi\eta_0)$ , where the reference Sommerfeld parameter  $\eta_0$  is calculated at 75 MeV) are compared to the low-energy data [7, 11]. The curves show in increasing order the no-coupling limit, and coupled-channels results obtained with different transfer strengths, namely,  $F_{1n} = 0$  (exc), 0.95 (exc+ntr-95), and 1.2 (exc+ntr-120).

the lowest energies. The calculation which includes the effect of transfer reproduces the low energy data very well, whereas the calculation which is based on couplings to excited states only falls off too steeply.

A good way to emphasize the low-energy behavior of the fusion cross section is to plot the  $S$  factor [10] for fusion,

$$S = E_{c.m.} \sigma_f(E_{c.m.}) \exp(2\pi\eta), \quad (5)$$

where  $\eta = Z_1 Z_2 e^2 / (\hbar v_{rel})$  is the Sommerfeld parameter, and  $v_{rel}$  is the asymptotic relative velocity in the entrance channel of the reacting nuclei. The  $S$  factors we obtain are shown in Fig. 6. It is seen that the calculation ‘exc’, which includes couplings to surface excitations, makes a very poor fit to the data around 70 MeV. The calculation ‘exc+ntr-120’, which in addition to surface excitations includes couplings to one-neutron transfer with the strength  $F_{1n} = 1.2$ , makes a surprisingly good fit. It is evident that couplings to transfer channels, in combination with the M3Y+repulsion potential, play a crucial role in explaining the fusion data at the lowest energies. Calculations that are based on the AW potential, on the other hand, do a very poor job at low energies (see Fig. 2A), and the quality of the fit to the data shows very little sensitivity to the transfer strength according to Table II.

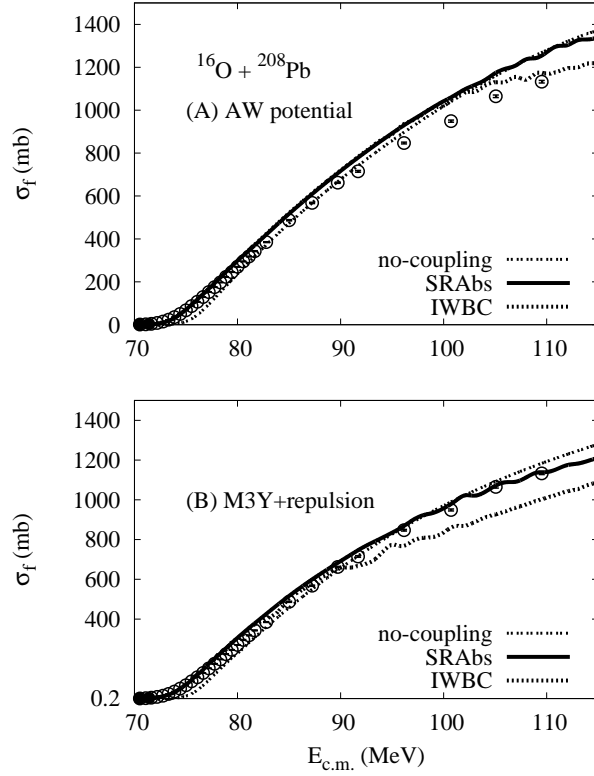


FIG. 7: Linear plot of fusion cross sections obtained with the AW potential (A) and the M3Y+repulsion potential (B). The no-coupling limits (thin dashed curves) are compared to data [7] and to coupled-channels calculations (exc+ntr, using  $F_{1n} = 0.95$ ). The fusion obtained from IWBC (dashed curves) is supplemented with the absorption from a short-ranged imaginary potential (SRAbs, solid curves).

### E. Fusion at high energies

The behavior of fusion at high energies is illustrated in Fig. 7 which shows a linear plot of the cross sections obtained using the AW potential (A) and the M3Y+repulsion potential (B). The no-coupling limit which is based on the AW potential (Fig. 7A) is seen to exceed the data at the highest energies. This is consistent with the analysis in Ref. [12] which showed that the fusion data are suppressed at high energy. This problem was fixed as mentioned earlier by using a large diffuseness of the ion-ion potential [7, 12].

The no-coupling limit which is based on the M3Y+repulsion potential is shown in Fig. 7B. It is in much better agreement with the data at the highest energies. Thus the application of the M3Y+repulsion potential seems to help resolve the problem of the suppression of the

high-energy fusion data. There is, however, another problem at high energy, namely, that the fusion cross sections obtained in coupled-channels calculations from the IWBC tend to drop far below the no-coupling limit and even below the data. This trend is clearly seen in Fig. 7B.

We have chosen to fix the problem with the IWBC in coupled-channels calculations at high energies by supplementing the ion-ion potential with a short-ranged imaginary potential that acts near the location  $R_{\text{pocket}}$  of the minimum of the pocket in the entrance channel potential. (We use the Woods-Saxon parameters:  $W_0 = -10$  MeV,  $a_w = 0.1$  fm,  $R_w = R_{\text{pocket}}$ .) It is seen that this prescription produces a cross section (solid curves in Fig. 7) that is closer to the no-coupling limit. Moreover, the agreement with the data is very good when we apply the M3Y+repulsion potential (Fig. 7B), whereas the data are suppressed when compared to the calculations that are based on the AW potential (Fig. 7A).

It is unfortunate that we have to resort to a short-ranged imaginary potential in order to be able to reproduce the high-energy fusion data because this prescription does not work at extreme subbarrier energies. We demonstrated that in section VII.A of Ref. [16] and it is also true for the  $^{16}\text{O}+^{208}\text{Pb}$  fusion reactions. At the moment we are only able to reproduce the hindrance of fusion at extreme subbarrier energies when we use IWBC without any imaginary potential.

Evidently, the behavior of the high energy fusion cross section is not trivial. That may not be so surprising because it is also difficult to reproduce the total reaction cross section and the elastic scattering at high energy, without making resort to some kind of absorption. Another problem is that the rotating frame approximation which we have used is unrealistic at large angular momenta because it ignores completely the angular momentum dissipation which together with the energy dissipation can be critical for high energy fusion. The qualitative influence of angular momentum dissipation is nicely illustrated in Fig. 18 of Ref. [25].

The quality of the fits to the data is illustrated in Fig. 8 in terms of the ratio of the measured and calculated fusion cross sections. The three coupled-channels calculations were all based on the M3Y+repulsion potential and they have been shifted by the energy  $\Delta E$  which is given in Table II, in order to produce the best  $\chi^2/N$ . This requirement tends to force the calculations to be in good agreement with the high energy data, because the statistical error is very small at high energy. It is only when we use the AW potential that

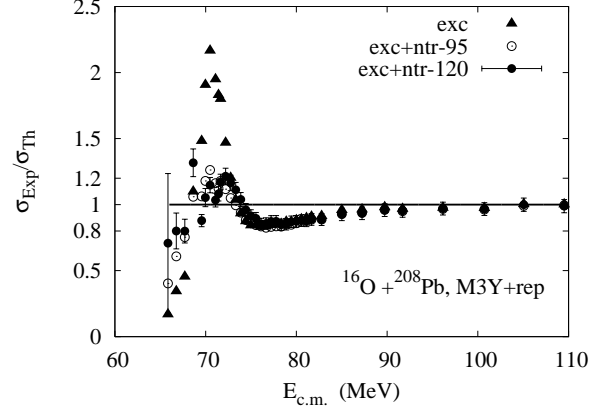


FIG. 8: Ratio of the measured and calculated fusion cross sections. The calculations are based on the M3Y+repulsion potential. They include couplings to surface excitations (exc), and to surface excitations and one-neutron transfer using the coupling strengths  $F_{1n} = 0.95$  (exc+ntr-95) and 1.2 (exc+ntr-120).

we see a suppression of the data at high energy (c.f. Fig. 7A). Thus we conclude that using the M3Y+repulsion potential not only explains the fusion hindrance phenomenon at low energies but it also helps eliminate the suppression of fusion that was observed in Ref. [12] at high energies.

The main discrepancy between experimental and calculated cross sections occurs in Fig. 8 at energies slightly below and slightly above the Coulomb barrier, which is located at  $V_{CB} = 75.6$  MeV. The enhancement of the ratio  $\sigma_{\text{exp}}/\sigma_{\text{cal}}$  just below the barrier is very sensitive to which calculation we compare to. The reduction of the ratio just above the barrier, on the other hand, is rather insensitive to the calculation we consider.

It is not clear how one can eliminate the deviation of the cross section ratio from unity. While the enhancement in Fig. 8 below the Coulomb barrier can be reduced by various means (by changing the coupling strengths, the number of channels, or by adjusting the ion-ion potential) the suppression above the barrier seems to be more robust. We note that the suppression above the barrier is closely related to the large peak height of the calculated barrier distributions shown in Fig. 5.



## IV. CONCLUSION

We have shown that the hindrance of fusion, which has recently been observed in  $^{16}\text{O}+^{208}\text{Pb}$  reactions at low energies, is consistent with the shallow pocket in the entrance channel potential which is produced by the M3Y+repulsion double-folding potential. There is strong evidence that couplings to transfer channels play a crucial role in explaining the energy dependence of the fusion cross section (or  $S$  factor) at the lowest energies.

The influence of couplings to transfer reactions in coupled-channels calculations of the  $^{16}\text{O}+^{208}\text{Pb}$  fusion has been recognized before [1, 2, 3] but the importance is much more dramatic when the new low-energy fusion data [7] are considered and the coupled-channels calculations are based on the shallow M3Y+repulsion potential. The best agreement with the fusion data is achieved by boosting the neutron transfer coupling strength so that the calculations reproduce the measured total reaction cross sections. This is a nice consistency check of the coupled-channels calculations.

Another way to account for the observed reaction cross sections is to employ an imaginary potential, and this made it possible for us to reproduce the elastic scattering data, at least at energies close to the Coulomb barrier. There are still some problems in accounting for the scattering data at energies far above the Coulomb barrier, and the fusion, which we usually define in terms of in-going wave boundary conditions, has to be supplemented with the absorption in a short-ranged imaginary potential at high energies in order to be able to simulate the data. Using this prescription at high energies, we are able reproduce the fusion data over eight orders of magnitude, from 10 nb to 1 b, with an average (root-mean-square) deviation of the order of 12%. It is a challenge to theory to reduce this deviation further.

Since the coupling to transfer plays such a prominent role in the fusion of  $^{16}\text{O}+^{208}\text{Pb}$  at very low energies, it may be useful in future work to reexamine the transfer form factors we have used. They were developed for peripheral reactions (much the same way the Akyüz-Winther potential was developed to describe the elastic scattering in peripheral collisions) but they may not be realistic at shorter distances between the reacting nuclei.

### Acknowledgments

We are grateful to B. B. Back, M. Dasgupta, and C. L. Jiang for discussions and encouragement. This work was supported (H.E.) by the U.S. Department of Energy, Office of Nuclear Physics, under Contract No. DE-AC02-06CH11357.

## V. APPENDIX: DENSITY PARAMETRIZATION

The matter or charge density of nuclei is often parametrized as  $\rho_0 f((r - R)/a)$  in terms of the Fermi function  $f(x) = 1/(1 + \exp(x))$ . For analytic purposes it is convenient to use instead the symmetrized form

$$\begin{aligned}\rho(r) &= \rho_0 f((r - R)/a) \cdot f(-(r + R)/a) \\ &= \frac{\frac{1}{2}\rho_0 \exp(R/a)}{\cosh(r/a) + \cosh(R/a)}.\end{aligned}\tag{6}$$

The radial shape is essentially the same as that of the normal Fermi function, when  $R$  is much greater than  $a$ . The largest modification is at  $r = 0$ , where the ordinary Fermi function is multiplied by the factor  $1/(1 + \exp(-R/a))$ .

A useful integral in this connection is

$$\begin{aligned}I(k) &= \int_0^\infty dr \cos(kr) \rho(r) \\ &= \frac{\rho_0 \exp(R/a)}{2 \sinh(R/a)} \frac{a\pi \sin(kR)}{\sinh(ka\pi)},\end{aligned}\tag{7}$$

which follows from Eq. 3.983 no. 1 or no. 2 in Ref. [26]. One can also invert this expression

$$\rho(r) = \frac{2}{\pi} \int_0^\infty dk \cos(kr) I(k).\tag{8}$$

These are the one-dimensional Fourier transform relations between  $\rho(r)$  and  $I(k)$ .

The three-dimensional Fourier transform of  $\rho(r)$  can easily be derived from Eq. 7,

$$\begin{aligned}\rho(\mathbf{k}) &= \int d\mathbf{r} \exp(-i\mathbf{k}\mathbf{r}) \rho(r) \\ &= \frac{4\pi}{k} \int_0^\infty dr r \sin(kr) \rho(r) = -\frac{4\pi}{k} \frac{dI(k)}{dk}.\end{aligned}\tag{9}$$

Inserting the derivative of (7) we obtain

$$\begin{aligned}\rho(\mathbf{k}) &= \frac{4\pi\rho_0 \exp(R/a)}{2 \sinh(R/a)} \frac{a\pi}{k} \times \\ &\quad \frac{a\pi \sin(kR) \cosh(ka\pi) - R \cos(kR) \sinh(ka\pi)}{(\sinh(ka\pi))^2}.\end{aligned}\tag{10}$$

A similar expression was derived in Ref. [27], Eq. (3-8j). It differs from Eq. (10) by the factor  $\exp(R/a)/[2 \sinh(R/a)]$ , which is usually close to one. The trick in deriving the analytic expression, Eq. (10), was to use the symmetrized density distribution, Eq. (6).

The overall normalization of the density in terms of the mass number  $A$  can be determined from Eq. (10) evaluated at  $\mathbf{k} = \mathbf{0}$ ,

$$A = \rho(\mathbf{k} = \mathbf{0}) = \frac{4\pi\rho_0 \exp(R/a)}{2 \sinh(R/a)} \frac{R^3}{3} \left(1 + \left(\frac{\pi a}{R}\right)^2\right). \quad (11)$$

The mean square radius of the ground state density can be extracted from the  $k^2$  term in the expansion of  $\rho(\mathbf{k})$ ,

$$\rho(\mathbf{k}) = A\left(1 - \frac{1}{6}k^2 \langle r^2 \rangle + \dots\right).$$

This yields the familiar result, Eq. (2-65) of Ref. [28],

$$\langle r^2 \rangle = \frac{3}{5} (R^2 + \frac{7}{3} (a\pi)^2). \quad (12)$$

- 
- [1] S. C. Pieper, M. J. Rhodes-Brown, and S. Landowne, Phys. Lett. **B162**, 43 (1985).
  - [2] I. J. Thompson, M.A. Nagarajan, J.S. Lilley, and B.R. Fulton, Phys. Lett. **B157**, 250 (1985).
  - [3] I. J. Thompson, M. A. Nagarajan, J. S. Lilley, and M. J. Smithson, Nucl. Phys. **A505**, 84 (1989).
  - [4] F. Videbaek, R. B. Goldstein, L. Grodzins, S. G. Steadman, T. A. Belote, and J. D. Garrett, Phys. Rev. C **15**, 954 (1977).
  - [5] E. Vulgaris, L. Grodzins, S. G. Steadman, and R. Ledoux, Phys. Rev. C **33**, 2017 (1986).
  - [6] C. R. Morton, D. J. Hinde, J. R. Leigh, J. P. Lestone, M. Dasgupta, J. C. Mein, J. O. Newton, and H. Timmers, Phys. Rev. C **52**, 243 (1995).
  - [7] C. R. Morton, A. C. Berriman, M. Dasgupta, D. J. Hinde, J. O. Newton, K. Hagino, and I. J. Thompson, Phys. Rev. C **60**, 044608 (1999).
  - [8] Ş. Mişicu and H. Esbensen, Phys. Rev. Lett. **96**, 112701 (2006).
  - [9] C. L. Jiang *et al.*, Phys. Rev. Lett. **93**, 012701 (2004).
  - [10] C. L. Jiang, B. B. Back, H. Esbensen, R. V. F. Janssens, and K. E. Rehm, Phys. Rev. C **73**, 014613 (2006).
  - [11] M. Dasgupta, D. J. Hinde, C. Low, and J. O. Newton, AIP Conference Proceedings **853**, 21 (2006); M. Dasgupta, D. J. Hinde, A. Diaz-Torres, B. Bouriquet, Catherine I. Low, G. J. Milburn, and J. O. Newton, Phys. Rev. Lett. **99**, 192701 (2007).
  - [12] J. O. Newton *et al.*, Phys. Lett. **B586**, 219 (2004).

- [13] S. C. Pieper, M. H. Macfarlane, D. H. Gloeckner, D. G. Kovar, F. D. Becchetti, B. G. Harvey, D. L. Hendrie, H. Homeyer, J. Mahoney, F. Pühlhofer, W. von Oertzen, and M. S. Zisman, *Phys. Rev. C* **18**, 180 (1978).
- [14] H. Esbensen and S. Landowne, *Nucl. Phys.* **A492**, 473 (1989).
- [15] H. Esbensen, C. L. Jiang, and K. E. Rehm, *Phys. Rev. C* **57**, 2401 (1998).
- [16] Ş. Mişicu and H. Esbensen, *Phys. Rev. C* **75**, 034606 (2007).
- [17] R. A. Broglia and Aage Winther, *Heavy-ion Reactions*, Lecture Notes Addison-Wesley (Redwood City CA, 1991).
- [18] H. De Vries, C. W. Jaeger, and C. De Vries, *At. Data and Nucl. Data Tables* **36**, 495 (1987).
- [19] K. T. Knöpfle, G. J. Wagner, H. Breuer, M. Rogge, and C. Mayer-Böricke, *Phys. Rev. Lett.* **35**, 779 (1975).
- [20] Evaluated Nuclear Structure Data Files, National Nuclear Data Center, Brookhaven National Laboratory; <http://www.nndc.bnl.gov/>
- [21] P. Raghaven, *At. Data Nucl. Data Tables* **42**, 189 (1989).
- [22] R. A. Broglia, C. H. Dasso, S. Landowne, and A. Winther, *Phys. Rev. C* **27**, 2433(R) (1983).
- [23] J. M. Quesada, G. Pollarolo, R. A. Broglia, and A. Winther, *Nucl. Phys.* **A442**, 381 (1985).
- [24] N. Rowley, G. R. Satchler, and P. H. Stelson, *Phys. Lett. B* **254**, 25 (1990).
- [25] R. Bock *et al.*, *Nucl. Phys.* **A388**, 334 (1982).
- [26] I. S. Gradshteyn and I. M. Ryzhik, *Table of Integrals, Series and Products* (Academic Press, New York and London, 1965).
- [27] Herbert Überall, *Electron Scattering from Complex Nuclei* (Academic Press, New York and London, 1971).
- [28] Aage Bohr and Ben R. Mottelson, *Nuclear Structure Vol. I* (Benjamin, New York, 1969).